Properties of HI discs in the Auriga cosmological simulations

Federico Marinacci[1]⋆, Robert J. J. Grand[2,3], Rüdiger Pakmor[2], Volker Springel[2,3],
Facundo A. Gómez[4], Carlos S. Frenk[5] and Simon D. M. White[4]

[1] *Kavli Institute for Astrophysics and Space Research, Massachusetts Institute of Technology, Cambridge, MA 02139, USA*
[2] *Heidelberger Institut für Theoretische Studien, Schloss-Wolfsbrunnenweg 35, 69118 Heidelberg, Germany*
[3] *Zentrum für Astronomie der Universität Heidelberg, ARI, Mönchhofstrasse 12-14, 69120 Heidelberg, Germany*
[4] *Max-Planck-Institut für Astrophysik, Karl-Schwarzschild-Str. 1, D-85748, Garching, Germany*
[5] *Institute for Computational Cosmology, Department of Physics, Durham University, South Road, Durham, DH1 3LE, UK*

ABSTRACT

We analyse the properties of the HI gas distribution in the Auriga project, a set of magnetohydrodynamic cosmological simulations performed with the moving-mesh code AREPO and a physics model for galaxy formation that succeeds in forming realistic late-type galaxies in the 30 Milky Way-sized haloes simulated in this project. We use a simple approach to estimate the neutral hydrogen fraction in our simulation set, which treats low-density and star-forming gas separately, and we explore two different prescriptions to subtract the contribution of molecular hydrogen from the total HI content. The HI gas in the vast majority of the systems forms extended discs although more disturbed morphologies are present. Notwithstanding the general good agreement with observed HI properties – such as radial profiles and the mass-diameter relation – the Auriga galaxies are systematically larger and more gas-rich than typical nearby galaxies. Interestingly, the amount of HI gas outside the disc plane correlates with the star formation rate, consistent with a picture where most of this extra-planar HI gas originates from a fountain-like flow. Our findings are robust with respect to the different assumptions adopted for computing the molecular hydrogen fraction and do not vary significantly over a wide range of numerical resolution. The HI modelling introduced in this paper can be used in future work to build artificial interferometric HI data cubes, allowing an even closer comparison of the gas dynamics in simulated galaxies with observations.

Key words: methods: numerical – galaxies: evolution – galaxies: fundamental parameters – galaxies: ISM – galaxies: structure – galaxies: evolution

1 INTRODUCTION

Cold gas plays a key role in the evolution of galaxies, in particular in those that are still actively forming stars like our own Milky Way. Indeed, the presence of a cold gas reservoir is necessary for a galaxy to keep forming stars (e.g. Sancisi et al. 2008, and references therein). Moreover, several pieces of evidence (Twarog 1980; Chiappini et al. 1997, 2001; Aumer & Binney 2009) indicate that some process of accretion, replacing the gas consumed by star formation with fresh (and possibly metal-poor) material, must be ongoing for a substantial fraction of the lifetime of a star-forming galaxy.

A very important component of this cold gas phase is represented by atomic hydrogen (HI). Radio observations of HI in nearby galaxies now date back several decades (Roberts 1975) and have been instrumental to study the kinematics (e.g. Verheijen & Sancisi 2001), structure (e.g. Broeils & Rhee 1997) and gaseous content (e.g. Catinella et al. 2013) of (late-type) galaxies (see also

Giovanelli & Haynes 2016, for an updated review on HI surveys). As the sensitivity of these observations improved with time (Heald et al. 2011; Kalberla et al. 2005; Wang et al. 2013), it has become possible to detect fainter and fainter HI structures, which has not only allowed a better census of the total HI content in spiral galaxies but also elucidated the interactions they have with their environment and their importance for galactic evolution. For example, the detection of extra-planar gas layers (i.e. low-column density HI gas that extends well outside the plane of the galactic disc, see e.g. Oosterloo et al. 2007) and the study of their kinematics (Fraternali 2009, and references therein) has revealed the interplay between the disc and the circumgalactic medium in late-type galaxies (Fraternali & Binney 2008; Marinacci et al. 2010, 2011). This interaction is mediated by a so-called galactic fountain (Shapiro & Field 1976; Houck & Bregman 1990) – which in the Milky Way manifests itself through intermediate-velocity (IVC) and high-velocity (HVC) clouds (Fraternali et al. 2015; Marasco & Fraternali 2011; Wakker & van Woerden 1997; Wakker 2004) – and provided indi-

⋆ E-mail: fmarinac@mit.edu

rect evidence of how star formation can be sustained for a Hubble time in these systems (Fraternali 2014).

The reproduction of the content and distribution of Hi gas in theoretical models of galaxy formation is of primary importance, given its key role in shaping galactic evolution. In fact, the numerous constraints posed by such observations represent a challenging test for any galaxy formation model. This is particularly true in hydrodynamical simulations, in which, due to the huge dynamic range in spatial scales that needs to be covered, many of the physical processes crucial for forming realistic objects are included in an approximate sub-grid fashion. The latter may in principle introduce a substantial uncertainty in the final results, and also an explicit dependence on the details of the numerical implementation of the sub-grid processes, calling for a validation against observations.

Some work in this direction has already been carried out, both in idealized set-ups and in full cosmological settings. These efforts mostly focused on the dependence on supernova feedback – a key process in galaxy formation models, especially for galaxies with virial masses up to $\sim 10^{12}\,\mathrm{M_\odot}$ – of the extra planar Hi distribution and kinematics in idealized Milky Way type galaxies (Marasco et al. 2015), and of the global Hi properties in full cosmological set-ups (e.g. Davé et al. 2013; Popping et al. 2009; Rahmati et al. 2013; Walker et al. 2014). However, the majority of this earlier cosmological work featured a simulated galaxy population with properties that are in substantial tension with observations, even when matching the large-scale Hi observational constraints. In particular, the simulated galaxies invariably exhibited too high stellar masses and lacked a well-defined disc component, due to an overly efficient cooling of baryons at the centre of dark matter haloes (the so-called 'over-cooling' problem, e.g. Navarro & Steinmetz 1997).

It was not until recently that this issue has been successfully addressed, essentially by invoking a more efficient coupling of the feedback energy – both stellar and, at the high $\gtrsim 10^{12}\,\mathrm{M_\odot}$ mass end, from active galactic nuclei – with the cooling gas. This more effective coupling can be very difficult to numerically resolve in full-scale cosmological simulations, and different groups have explored various approaches to address this problem. Notwithstanding these technical difficulties, there are now several simulation methodologies that are able to produce realistic looking galaxies in hydrodynamic cosmological simulations both in uniformly-sampled boxes – as for instance in the Illustris (Vogelsberger et al. 2014a,b) and EAGLE (Schaye et al. 2015) simulation projects – and in configurations that focus on the formation of a single object, commonly a Milky Way-sized galaxy (e.g. Aumer et al. 2013; Colín et al. 2016; Guedes et al. 2011; Marinacci et al. 2014a; Stinson et al. 2013; Wang et al. 2015), or a region of prespecified density (McCarthy et al. 2012).

The availability of a new generation of cosmological simulations yielding realistic galaxies implies that it is now possible to study their Hi content and kinematics more reliably than possible in the past (for very recent analysis see Crain et al. 2016; Macciò et al. 2016; Marasco et al. 2016), and also to check whether the increased feedback efficiency, which nominally should significantly affect the gas properties within and in the vicinity of the star forming disc, has an effect on the (global) distribution of the Hi gas. This has been explored in the context of the EAGLE collaboration by Bahé et al. (2016, hereafter B16), who have analysed several properties of the Hi gas – including morphologies, radial distribution, gas fractions, Hi masses and sizes – of the simulated galaxy set. In their study, B16 conclude that the increased efficiency of the stellar feedback and its local character have indeed a large impact on the morphology of the Hi discs, and strongly influences its radial

distribution. Other properties, such as Hi masses and sizes, appear to be less sensitive to the increased (stellar) feedback efficiency.

Similarly to the work of B16, in this paper we present an analysis of the Hi properties of a set of 30 cosmological zoom-in magneto-hydrodynamic (MHD) simulations of disc galaxy formation, named the Auriga simulations, performed with the moving-mesh code AREPO and a state-of-the-art model of galaxy formation physics largely based on the one used for the Illustris project (see Vogelsberger et al. 2013), slightly adapted for zoom-in simulations of Milky Way type objects (Marinacci et al. 2014a). Compared to the study of B16 the zoom-in technique makes it possible to reach a finer (mass and spatial) resolution in Auriga – by factors of about 36 in mass and 3 in gravitational softening length compared to the fiducial resolution of EAGLE – and the relatively large number of simulated haloes allows us to draw statistically meaningful conclusions about the properties of the resulting Hi discs, albeit limited to halo masses around $\simeq 10^{12}\,\mathrm{M_\odot}$ which is the range of masses chosen as Milky Way-like candidate haloes in the Auriga project. We note that the B16 and our simulation set have very different treatments for the star-forming gas and stellar feedback, enabling an interesting comparison on how the numerical implementation of these aspects impacts the simulated Hi distribution.

This paper is structured as follows. In Section 2, we briefly describe the main properties of the simulations that we have analysed in this study and the numerical techniques employed to carry them out. Section 3 presents the method that we have adopted to estimate the Hi content of the Auriga discs, and in particular gives details on the two prescriptions that we have used to treat the molecular gas fraction. In Section 4, we illustrate our main results focusing on the structural properties, scaling relations and gas content of the simulated Hi discs. These findings are compared to observations and with previous simulation results. Finally, in Section 5, we present our conclusions.

2   THE AURIGA SIMULATIONS

In this work, we investigate the Hi content of the cosmological hydrodynamical simulation suite Auriga (Grand et al. 2016a). This simulation suite is aimed at modelling the formation and evolution of Milky Way-like galaxies in their proper cosmological context. Full technical details about the simulation suite can be found in Grand et al. (2016a)[1]. In the following, we restrict ourselves to a concise description of the numerical methods adopted to run the simulations and their main properties.

The Auriga simulations follow a Λ cold dark matter cosmology with parameters $\Omega_\mathrm{m} = \Omega_\mathrm{dm} + \Omega_\mathrm{b} = 0.307$, $\Omega_\mathrm{b} = 0.048$, $\Omega_\Lambda = 0.693$, and Hubble constant $H_0 = 100\,h\,\mathrm{km\,s^{-1}Mpc^{-1}}$ = 67.77 km s^{-1}Mpc^{-1}, consistent with the Planck Collaboration XVI (2014) data release. The candidate haloes selected for resimulation were identified in a low-resolution simulation of a periodic cosmological box of side $100\,\mathrm{Mpc}$. Candidate haloes were selected in a virial mass range around $10^{12}\,\mathrm{M_\odot}$, consistent with recent determinations of the MW mass (Wilkinson & Evans 1999; Sakamoto et al. 2003; Battaglia et al. 2005; Dehnen et al. 2006; Li & White 2008; Xue et al. 2008; Peñarrubia et al. 2016), a mild isolation criterion – no object of more than half the mass of the candidate is allowed to be closer than $1.37\,\mathrm{Mpc}$ – was enforced at $z = 0$ to select relatively isolated objects.

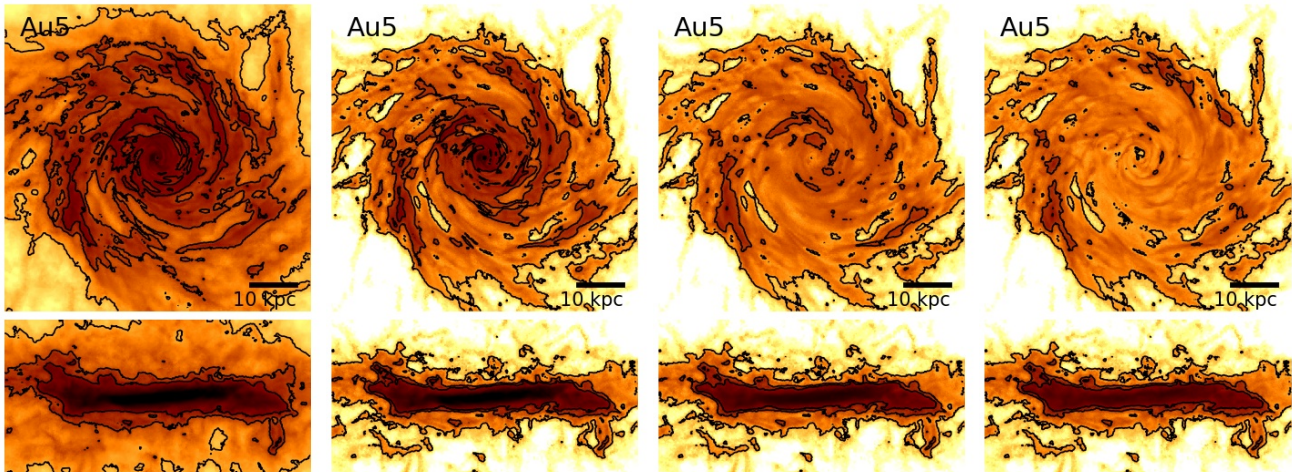**Figure 1.** HI projections. From left to right: total H density, neutral H density (HI + H$_2$), HI density from the L08 pressure prescription, HI density from the GK11 prescription. The size of the projected region is 50 kpc on a side for face on projections and 50×25 kpc for edge-on projections. To align the projections, the spin direction of the cold, star-forming gas within 10% of the virial radius of the halo has been used. The colour scale logarithmically maps the column densities in the interval $[5 \times 10^{18}, 10^{22}]\,\mathrm{cm}^{-2}$, and contour levels are placed at 10, 5 and 1 M$_\odot$ pc^{-2} from the inside to the outside.

The selected haloes (denoted with the acronym Au i, where i is the halo ID) were simulated multiple times at different resolution levels by applying the so-called "zoom-in" technique, in which the mass distribution in the Lagrangian region that forms the main halo is sampled by a large number of resolution elements, whereas progressively coarser resolution is applied with increasing distance from the target object. At the fiducial resolution level that we are going to analyse in the present work (which from now on will be referred to as level 4), the typical baryonic mass resolution is $\sim 4 \times 10^4 \mathrm{M}_\odot$ and that of the dark matter component is $\sim 3 \times 10^5 \mathrm{M}_\odot$. The softening length of the dark matter particles is kept fixed in comoving space and allowed to grow in physical space up to a maximum of $369\,\mathrm{pc}$, while the gas softening length is scaled by the mean radius of the cell. The maximum physical softening allowed is $1.85\,\mathrm{kpc}$.

Gas was included in the initial conditions by adopting the same technique as in Marinacci et al. (2014a,b, and references therein). In practice, each particle in the initial conditions is split into a pair of a dark matter particle and a gas cell. The phase space coordinates of the pair are chosen such that its centre of mass and centre of mass velocity are equal to those of the original dark matter particle. The mass ratio of the pair is set by the cosmic baryon fraction, and the dark matter particle and gas cell are separated by a distance equal to half the mean inter-particle spacing.

The simulation suite was carried out using the moving-mesh, MHD code AREPO (Springel 2010). To solve for collisionless dynamics, AREPO employs a TreePM approach, in which the gravitational force is split into a long-range and a short-range component (see Springel 2005, for details). The long-range contribution is calculated on a Cartesian mesh via a Fourier method, while for the short-range component a gravitational oct-tree (Barnes & Hut 1986) is used. The MHD equations are discretized in a finite-volume approach on a dynamic unstructured Voronoi tessellation of the simulation domain. The special trait of AREPO, distinguishing it from other cosmological finite-volume codes, is that the mesh-generating points defining the Voronoi tessellation are allowed to move with the local fluid velocity, thereby giving rise to a quasi-Lagrangian numerical method which is manifestly Galilean-invariant. The MHD equations are solved with a second order

Runge-Kutta integration scheme complemented with least square spatial gradient estimators of primitive variables (Pakmor et al. 2016) and the Powell et al. (1999) eight-wave cleaning scheme to ensure the $\nabla \cdot \boldsymbol{B} = 0$ constraint.

The Auriga simulations use a galaxy formation physics model that accounts for the baryonic processes that play a key role in the formation of late-type galaxies. The model itself is an updated version of the one used in Marinacci et al. (2014a,b), which was specifically developed for large-scale cosmological simulations and whose free parameters were calibrated against a small set of observables such as the cosmic star formation history and the galaxy stellar mass function. For a full description of the implementation details we refer the reader to Vogelsberger et al. (2013). Differences of the present galaxy formation module with respect to the Marinacci et al. (2014a) implementation are discussed in Grand et al. (2016a).

Magnetic fields are included in the initial conditions as in Pakmor et al. (2014) by seeding a homogeneous B-field of 10^{-14} (comoving) G along the z-direction, which is then amplified due to the assembly of the main galaxy. The seeding is necessary because, in ideal MHD, B-fields cannot be self-consistently generated when starting from zero-field initial conditions. We note that previous cosmological MHD simulations with AREPO have shown that the results are essentially insensitive to the choice of both the intensity and the direction of the seed field (Pakmor et al. 2014), at least inside virialized structures (Marinacci et al. 2015) where any memory of the initial conditions is quickly erased due to vigorous, small-scale dynamo amplification of the field.

3 COMPUTATION OF THE HI MASS

The first step in our analysis is to estimate the amount of neutral atomic hydrogen contained in any given cell ($M_{\mathrm{HI},i}$) of our simulated objects, which can be expressed as follows

$$M_{\mathrm{HI},i} = (1 - f_{\mathrm{mol},i}) f_{\mathrm{neutr},i} X_i M_i, \qquad (1)$$

where M_i is the total gas mass contained in a given cell i, X_i is the hydrogen mass fraction, $f_{\mathrm{neutr},i}$ the neutral hydrogen fraction and

$f_{\mathrm{mol},i}$ the molecular hydrogen fraction, respectively. M_i and X_i are readily available from the simulation output, since AREPO directly tracks their evolution. The determination of the neutral H fraction $f_{\mathrm{neutr},i}$ and of the molecular H fraction $f_{\mathrm{mol},i}$ is, however, slightly more involved and require some additional modelling. We discuss the procedure that we have adopted to estimate these quantities in the following sections.

3.1 Estimate of the neutral gas fraction $f_{\mathrm{neutr},i}$

The gas cooling module in AREPO determines $f_{\mathrm{neutr},i}$ for each cell. This quantity is computed by modelling an ionization network for a mixture of hydrogen and helium (Katz et al. 1992, 1996). Two body processes (such as collisional excitation, collisional ionization, recombination, dielectric recombination and free–free emission) and Compton cooling off the cosmic microwave background (Ikeuchi & Ostriker 1986) are considered. In addition to these, the energy input due to a time-varying photoionizing UV background (Faucher-Giguère et al. 2009) is also taken into account. For a complete description of the gas cooling module and metal cooling treatment used in Auriga we refer the reader to Vogelsberger et al. (2013).

In principle, this information could be directly used in equation (1). However, in the galaxy formation model used in the simulations, gas above a predetermined density threshold, $n_{\mathrm{th}} \sim 0.13\,\mathrm{cm}^{-3}$, is eligible for star formation. This star-forming gas, in turn, is modelled by an effective equation of state describing a simplified ISM model comprising hot ($T \sim 10^7\,\mathrm{K}$) and cold ($T \sim 10^3\,\mathrm{K}$) gas phases in pressure equilibrium (see Springel & Hernquist 2003). Because the thermodynamic state of the gas is dictated by the effective equation of state, the value $f_{\mathrm{neutr},i}$ estimated by the code for the star-forming gas is unreliable for our purposes.

As stated above, the cold gas phase, which is one of the constituents of our ISM model, has a temperature around 10^3 K and as such we expect that the gas comprising it is essentially neutral. Therefore, it is natural to assume that for star-forming gas, $f_{\mathrm{neutr},i}$ is simply the mass fraction of the cold gas phase of our ISM, which can be easily determined as (see Springel & Hernquist 2003)

$$x = \frac{u_h - u}{u_h - u_c}, \qquad (2)$$

where $u = P/[(\gamma - 1)\rho]$ is the gas thermal energy per unit mass (set by the effective equation of state), and u_c and u_h are the gas thermal energy of the cold and the hot ISM phase, respectively. In what follows we will thus use for $f_{\mathrm{neutr},i}$ the value estimated from equation (2) if the gas is star-forming, or otherwise the value directly computed by the AREPO cooling module for gas densities below the star formation threshold n_{th}.

3.2 Treatment of the molecular gas

Once $f_{\mathrm{neutr},i}$ has been determined, the contribution of the atomic hydrogen must be separated from the molecular phase. The galaxy formation physics modules currently employed in AREPO do not directly account for the mechanisms responsible for the creation and destruction of molecular hydrogen. Therefore, we adopt two phenomenological methods to achieve this objective, also with the goal to investigate systematic differences arising from the specific treatment of molecular hydrogen in our analysis (see Section 4 for more details).

The first method is purely empirical and is based on a set of observations of nearby galaxies (Leroy et al. 2008, hereafter L08).

As originally proposed by Blitz & Rosolowsky (2006), it consists of fitting the ratio R_{mol} between the column density of molecular over atomic hydrogen with the functional form

$$R_{\mathrm{mol}} = \left(\frac{P}{P_0} \right)^\alpha, \qquad (3)$$

where P is the gas mid-plane pressure and P_0 and α are free parameters. In our case, we take R_{mol} in equation (3) as the ratio between the molecular and atomic hydrogen volumetric densities and P as the gas pressure[2] in any given cell. The molecular fraction can then be easily obtained as

$$f_{\mathrm{mol},i} = \frac{R_{\mathrm{mol},i}}{R_{\mathrm{mol},i} + 1}, \qquad (4)$$

once the value of P_0 and α have been fixed. Following L08 we choose $P_0 = 1.7 \times 10^4\,\mathrm{K\,cm}^{-3}$ and $\alpha = 0.8$. We explicitly checked that using the parametrization proposed by Blitz & Rosolowsky (2006) does not alter our findings significantly.

The second method is more theoretically motivated and is based on the work by Gnedin & Kravtsov (2011, hereafter GK11). Following Lagos et al. (2015, Appendix A1) we define

$$f_{\mathrm{mol},i} = \left(1 + \frac{\Sigma_c}{\Sigma_{\mathrm{neutr},i}} \right)^2, \qquad (5)$$

where $\Sigma_{\mathrm{neutr},i}$ is the neutral hydrogen column density and Σ_c is a critical column density given by

$$\Sigma_c = 20\,\mathrm{M}_\odot\,\mathrm{pc}^{-2} \frac{\Lambda(D_{\mathrm{MW}}, G_0')^{4/7}}{D_{\mathrm{MW}}\sqrt{1 + G_0'\,D_{\mathrm{MW}}^2}}. \qquad (6)$$

In the previous expression, D_{MW} is the dust-to-gas mass ratio normalized to the Milky Way value and estimated as $D_{\mathrm{MW}} \equiv Z_i/Z_\odot$, where Z_i is the metallicity of the gas cell, $Z_\odot = 0.0127$, G_0' is the interstellar radiation field in units of the Habing (1968) radiation field, and $\Lambda(D_{\mathrm{MW}}, G_0')$ is a fitting function depending on the latter two variables (see GK11; Lagos et al. 2015, for more details). As in Lagos et al. (2015), G_0' is expressed in terms of the star formation rate (SFR) density in the solar neighbourhood as $G_0' = \Sigma_{\mathrm{SFR}}/\Sigma_{\mathrm{SFR},0}$, where $\Sigma_{\mathrm{SFR},0} = 10^{-3}\,\mathrm{M}_\odot\,\mathrm{yr}^{-1}\,\mathrm{kpc}^{-2}$ (Bonatto & Bica 2011). Column (surface) densities are computed by multiplying the relevant volumetric quantities by the Jeans length (see Schaye 2001)

$$\lambda_{\mathrm{J}} = \frac{c_{\mathrm{s}}}{\sqrt{G\,\rho}}, \qquad (7)$$

where c_{s} is the sound speed, G the gravitational constant, and ρ the total gas density. λ_{J} is computed individually for every cell. Finally, to protect against numerical divergences, a metallicity floor equal to $10^{-8}\,Z_\odot$ is imposed.

Fig. 1 illustrates the different steps of the procedure that we have just described when applied to halo Au 5. In particular, the panels from left to right can be thought of as the result of progressively applying the correcting factors (from the rightmost to the leftmost) used to determine the H I content listed in equation (1) to the total gas cell mass. They show, respectively, the projection both face on (top row) and edge on (bottom row) of the total H density

---

[2] We consider only the partial pressure of the cold gas phase, computed by multiplying the total gas pressure by the neutral gas fraction x in equation (2), for star-forming gas.
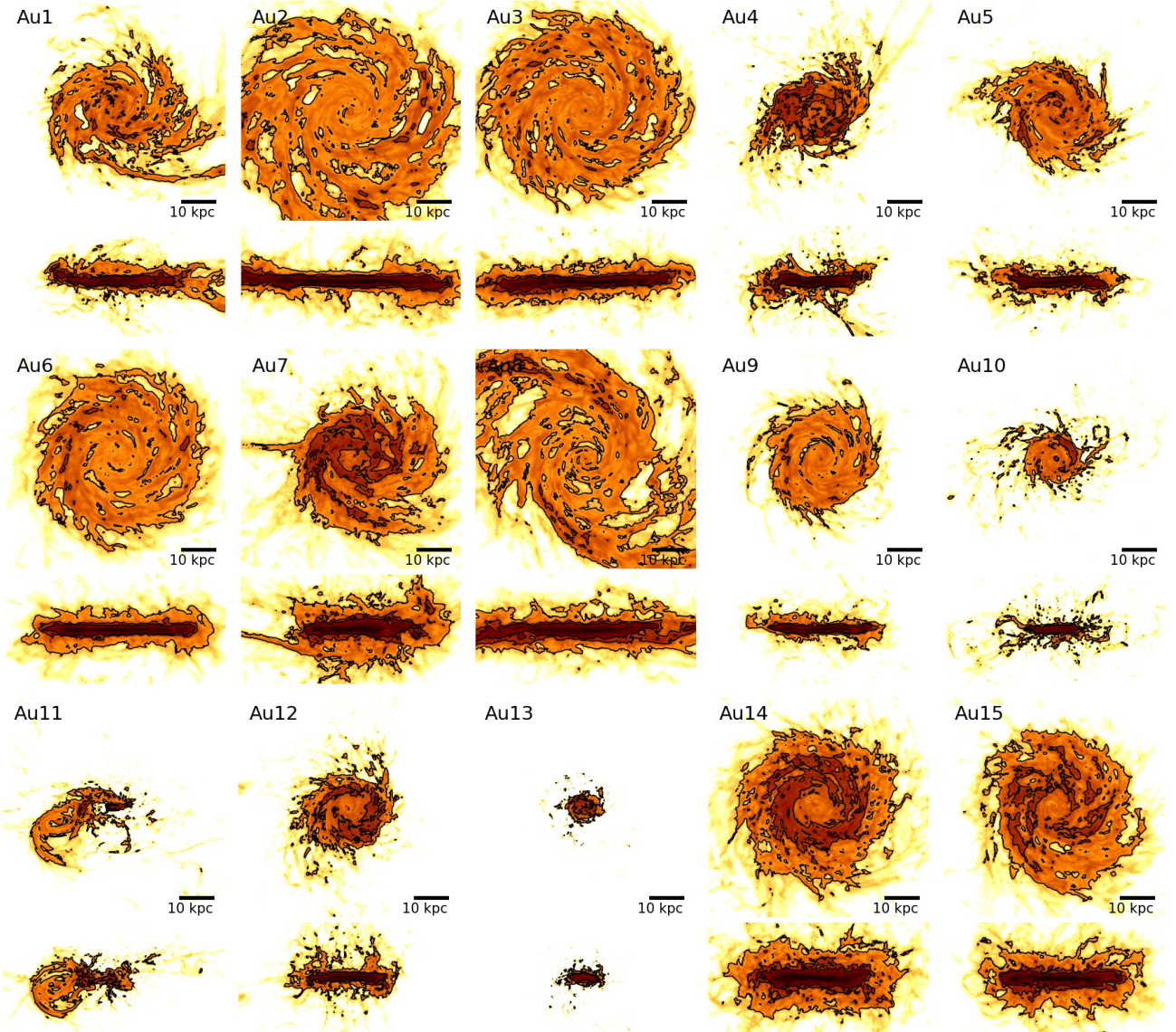
Figure 2. HI projections for haloes Au 1 to Au 15 obtained by using the L08 empirical relation to account for molecular gas. Each halo is shown face-on (top) and edge-on (bottom). The size of the projection region is 90 kpc on a side for face-on projections and 90×45 kpc for the edge-on views.

(including ionized gas), the neutral H density (HI + H$_2$) and the HI density obtained following the L08 and GK11 prescriptions.

It is readily apparent in these projections that the disc of neutral hydrogen in the Au 5 halo is surrounded by a much more extended layer of ionized gas. Removing the ionized layer leaves a gaseous disc that has about the same extent and external shape whether or not molecular hydrogen is taken into account. This is consistent with the picture that molecules form in the highest density regions (i.e. in the central regions of the simulated discs), and their importance to the mass budget contribution in the outskirts is negligible. The largest difference between the total (HI+ H$_2$) neutral hydrogen and HI column density is certainly in the centre (the innermost $\sim 10\,\mathrm{kpc}$), where the projected density drops by a factor of ~ 10. Although there is a very good resemblance in the main morphological features of the HI projection regardless of the method used to take into account the molecular gas, some minor differences are visible, and in particular the GK11 method yields consistently lower HI column densities in the central regions of the

simulated disc. As we will discuss more extensively later on, this appears to be a general trend and it is not limited to the particular halo that we have presented here.

4 RESULTS

4.1 HI morphologies

We start our analysis by presenting in Figs. 2 and 3 HI density projections for the set of 30 Auriga galaxies at redshift $z = 0$ obtained with the L08 method to estimate the molecular gas fraction. Both face-on (top panels) and edge-on projections (bottom panels) are presented. The gaseous discs are aligned by computing the spin axis of the dense, star-forming gas within 10% of the virial radius of each object. Each panel has the same physical size (90×90 kpc for face-on projections, and 90×45 kpc for the edge-on ones, with a depth of projection of 90 kpc in all cases) to facilitate the
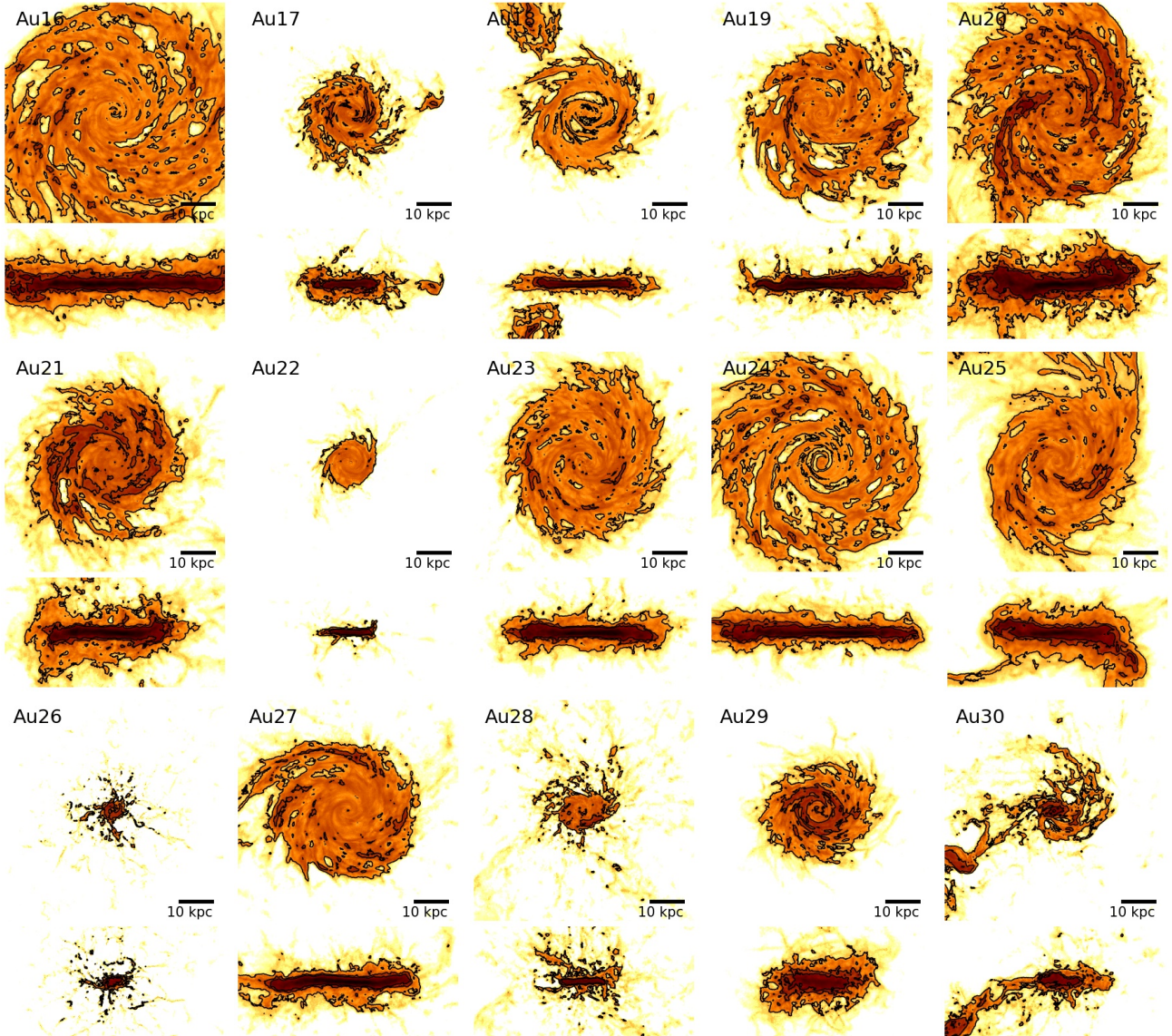
Figure 3. H I projections for haloes Au 16 to Au 30 obtained by using the L08 empirical relation to account for molecular gas. Each halo is shown face on and edge on. The size of the projection region is 90 kpc on a side for face-on projections and 90×45 kpc for the edge-on views.

size comparison among different objects, and is centred on the potential minimum of each simulated galaxy. The colour mapping, encoding column densities in the range $5 \times 10^{18} - 10^{22}\,\mathrm{cm}^{-2}$, is also kept the same in all panels for the same reason. Contours are placed at H I surface densities of 10, 5, and $1\,\mathrm{M}_\odot\,\mathrm{pc}^{-2}$ from the innermost to the outermost. We remind the reader that $1\,\mathrm{M}_\odot\,\mathrm{pc}^{-2} \simeq 1.249 \times 10^{20}\,\mathrm{cm}^{-2}$ for hydrogen.

In the majority of the systems, the H I gas is distributed in an extended disc (i.e. is more extended than the stellar component), which in some cases can reach galactocentric distances up to $\sim 60\,\mathrm{kpc}$ (e.g. Au 2, Au 16, Au 24). In the vertical direction, the thickness of the H I layer is very diverse. We have examples of relatively thin gaseous discs (e.g. Au 2, Au 9, Au 10, Au 18, Au 19, Au 23, Au 24) while others feature a very extended vertical distribution (Au 7, Au 14, Au 15, Au 21, Au 25, Au 29) that can reach tens of kpc outside the mid-plane. In the latter case, these vertically extended layers are often found in conjunction with a ring of more dense H I material or gas that is tracking spiral-like features in the

face-on projection. These features are much less frequent (and less prominent) for thinner H I discs. The vertical thickness can be of the order of $\sim 1.5 - 2\,\mathrm{kpc}$ for thin discs, while reaching $\sim 5\,\mathrm{kpc}$ for more extended structures (see Table 1). In Section 4.3 we discuss the calculation of the disc vertical thickness in more detail and relate it to the galactic fountain flows generated by stellar feedback.

A comparison between the H I morphologies obtained with the two prescriptions to determine the molecular gas fraction is presented in Fig. 4 (top row showing the L08, method and bottom row the GK11 method, respectively) for a few selected examples. In agreement with the results discussed in Section 3.2, the morphologies of the H I discs remain relatively unchanged. For example, their vertical and radial extent is only marginally affected by how the contribution of H_2 is calculated (see also Table 1 and Section 4.4 for a more quantitative analysis). The main difference is again in the central regions of the disc, where the GK11 approach predicts a lower H I fraction than the L08 method. This is illustrated by the decrease of the H I surface density, which sometimes, like in
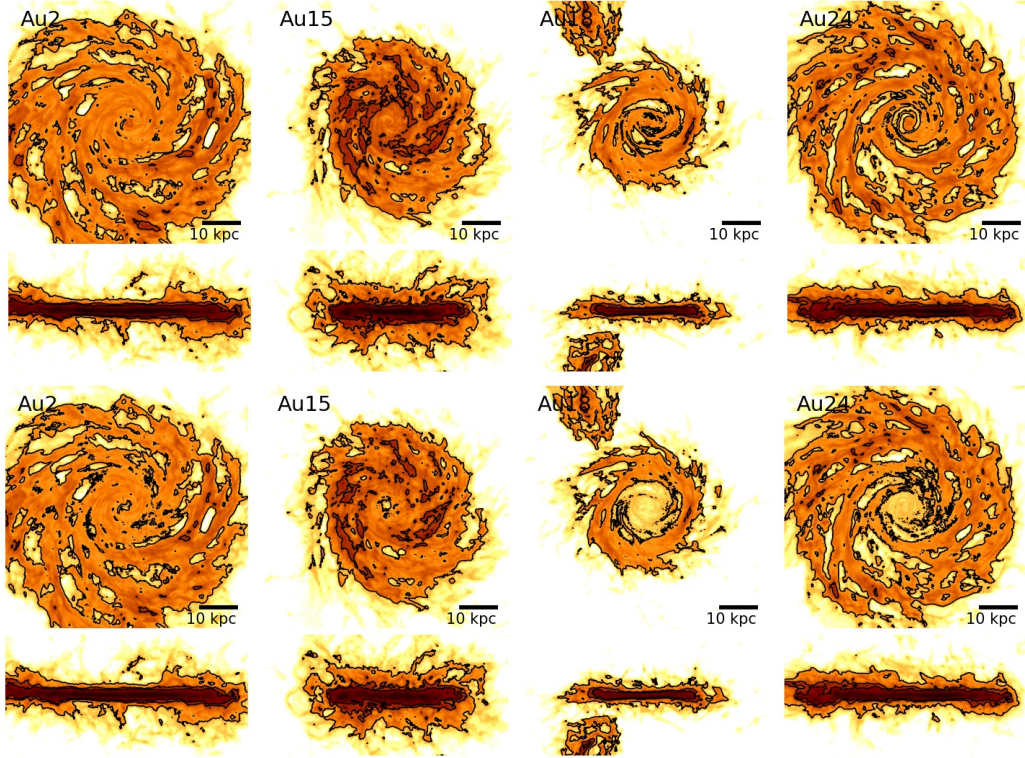
Figure 4. Comparison of the HI disc morphologies obtained by using the L08 (top row) and GK11 (bottom row) prescriptions to account for molecular gas for a selection of four Auriga haloes. Each halo is shown face-on and edge-on, with a size of the projection region of 90 kpc on a side for face-on projections and 90×45 kpc for edge-on projections.

Au 18 and Au 24, can be very pronounced and extend over large (~ 10 kpc) scales.

It is also informative to compare our HI morphology with that obtained in other cosmological simulations of galaxy formation, and in particular with the recent HI study of B16 based on the EAGLE simulations (Schaye et al. 2015). An interesting aspect of this comparison is that similar methods were used to estimate the HI fraction in both the EAGLE and Auriga simulations, whereas the two simulation sets differ in the implementation of the ISM physics – although they both use an effective equation of state for cold and dense gas (see Dalla Vecchia & Schaye 2012; Springel & Hernquist 2003, respectively) – and stellar feedback, as well as in the achieved resolution, which is about a factor of 36 better in mass for the Auriga runs. The main difference lies in the treatment of stellar feedback, which is local and more violent in EAGLE compared to the Auriga model. The latter employs a stochastic spawning of wind 'particles' that effectively gives rise to a non-local injection of supernova momentum (see Vogelsberger et al. 2013, for details). This has a significant impact on the HI morphologies. In the EAGLE simulations, unrealistically large holes of tens of kpc of size are clearly visible in the neutral gas distribution of some galaxies. This affects not only the morphologies of the HI discs, but also the radial gas distribution. Our simulations do not seem to suffer from the same problem, although gaps in the HI distribution can sometimes be seen, especially for the more extended HI discs (e.g. Au 2, Au 16, Au 24). To conclude, it is conceivable that some of the adverse effects on the HI distribution due to the nature of the stellar feedback used in the EAGLE simulation might be mitigated at higher resolution. Indeed, resolution is expected to have some impact on the efficiency (see Dalla Vecchia & Schaye 2012) and the

'granularity' (i.e. the number of gas particles heated per feedback event) of the stellar feedback in EAGLE, making it less violent and helping reducing the unphysically large sizes of the HI holes.

4.2 HI radial profiles

Figs 5 and 6 show azimuthally averaged HI surface density profiles as a function of the galactocentric radius for the 30 objects in the Auriga simulations. The galactocentric radii have all been expressed in terms of the azimuthally averaged HI radius of each object, defined as $\Sigma_{\mathrm{HI}}(R_{\mathrm{HI}}) = 1\,\mathrm{M}_\odot\,\mathrm{pc}^{-2}$ (see, e.g., Broeils & Rhee 1997, and Table 1 for their values). The profiles have been obtained by turning the HI disc face on (using again a direction defined by the angular momentum of the cold star-forming gas) and considering the gas cells in a rectangular box centred on the halo potential minimum and extending for 120 kpc perpendicular to the disc and for 240×240 kpc in the other directions. The gas cells in this region have been binned in 120 concentric annuli of 1 kpc width, and the surface density of each annulus has been computed by calculating the total HI mass of the annulus divided by its surface area. The figure shows the profiles for both the L08 (blue) and GK11 (red) method of computing the molecular fraction.

Although some variability is present between the different profiles, a general trend can be identified. Starting from the centre of the profile, the HI surface density increases up to a point where it reaches a plateau of approximately constant surface density. After this plateau, which in some cases (e.g. Au 2, Au 16, Au 20) can extend up to 10 kpc, Σ_{HI} drops quite rapidly, and very little HI is left past R_{HI}. The density plateau is not always present. Some profiles (e.g. Au 6, Au 12, Au 13, Au 14, Au 21, Au 26) in-

Run	$R_{\mathrm{HI}}^{\mathrm{L}}$ [kpc]	$M_{\mathrm{HI}}^{\mathrm{L}}$ [$10^9\,\mathrm{M_\odot}$]	$\Sigma_{\mathrm{HI}}^{\mathrm{L}}$ [$\mathrm{M_\odot\,pc^{-2}}$]	$h_{\mathrm{HI}}^{\mathrm{L}}$ [kpc]	$R_{\mathrm{HI}}^{\mathrm{GK}}$ [kpc]	$M_{\mathrm{HI}}^{\mathrm{GK}}$ [$10^9\,\mathrm{M_\odot}$]	$\Sigma_{\mathrm{HI}}^{\mathrm{GK}}$ [$\mathrm{M_\odot\,pc^{-2}}$]	$h_{\mathrm{HI}}^{\mathrm{GK}}$ [kpc]
			Fiducial resolution (level 4)					
Au 1	29.6	8.0	2.9	1.9	29.9	8.7	3.1	2.4
Au 2	49.9	22.3	2.8	1.7	50.0	22.0	2.8	1.8
Au 3	42.0	18.2	3.3	1.7	42.2	17.0	3.0	2.3
Au 4	22.7	7.3	4.5	2.7	23.5	7.6	4.4	4.9
Au 5	24.4	7.2	3.8	1.9	24.7	7.0	3.7	2.9
Au 6	38.0	15.0	3.3	1.6	38.2	14.8	3.2	1.9
Au 7	35.4	17.9	4.6	4.3	35.5	19.1	4.8	5.8
Au 8	54.8	22.1	2.3	1.8	55.1	22.9	2.4	1.9
Au 9	24.5	6.3	3.3	1.3	24.7	6.3	3.3	1.8
Au 10	13.2	2.2	3.9	1.7	13.6	2.4	4.1	4.1
Au 11	15.1	1.4	1.9	3.5	15.1	1.7	2.3	4.5
Au 12	19.8	6.6	5.3	2.2	20.2	7.0	5.5	4.8
Au 13	7.1	0.8	5.0	1.7	7.3	1.1	6.8	2.5
Au 14	34.6	21.4	5.7	4.5	34.8	21.2	5.6	6.2
Au 15	34.0	17.2	4.7	3.1	34.1	17.1	4.7	4.7
Au 16	52.2	29.2	3.4	2.0	52.3	29.2	3.4	2.4
Au 17	20.3	4.4	3.4	2.2	20.5	4.7	3.5	3.4
Au 18	25.0	5.0	2.5	1.2	25.1	4.6	2.3	1.5
Au 19	36.2	12.9	3.1	1.5	36.3	12.7	3.1	1.9
Au 20	46.9	29.3	4.3	3.7	47.1	30.8	4.4	4.3
Au 21	34.8	17.7	4.7	2.6	34.9	17.0	4.4	4.5
Au 22	11.2	1.4	3.6	1.0	11.3	1.4	3.4	1.5
Au 23	34.8	14.5	3.8	1.7	35.0	14.2	3.7	2.1
Au 24	43.9	18.3	3.0	1.3	44.0	18.0	2.9	1.7
Au 25	37.8	15.6	3.5	2.5	37.9	15.6	3.5	3.0
Au 26	5.6	0.5	5.0	3.7	5.9	0.7	6.7	10.4
Au 27	32.0	13.7	4.3	1.9	32.2	13.0	4.0	2.7
Au 28	14.7	1.9	2.9	4.8	14.9	2.1	3.0	9.2
Au 29	22.6	8.3	5.2	4.5	22.7	7.9	4.9	5.3
Au 30	18.0	2.5	2.4	2.7	19.1	2.8	2.4	3.8
			Low resolution (level 5)					
Au 16	61.1	39.1	3.3	3.4	61.4	40.8	3.5	3.4
Au 24	30.5	13.1	4.5	2.0	30.7	13.5	4.6	2.3
			High resolution (level 3)					
Au 16	57.9	27.2	2.6	1.6	58.2	26.6	2.5	2.3
Au 24	43.1	17.8	3.0	1.8	43.3	17.0	2.9	2.4

Table 1. Properties of HI discs in the Auriga simulations. The columns list (from left to right): simulation name; HI radius, HI mass, average HI surface density and HI vertical thickness (L08 method); HI radius, HI mass, average HI surface density and HI vertical thickness (GK11 method).

stead show an increase of Σ_{HI} up to a maximum value after which the profiles immediately decline. Other profiles (e.g. Au 11, Au 30) show a monotonic decrease of the HI surface density at all radii, but we note that this could be due to interactions with close, massive companions that they are currently experiencing.

It is also interesting to compare the difference in the HI radial profiles due to the two different methods that we have used to take into account the contribution of the molecular gas to the total neutral H density. In general, it can be seen that the two methods agree very well at large radii (i.e. $R \sim R_{\mathrm{HI}}$), where the contribution of molecular hydrogen to the total budget is negligible. The agreement still remains remarkable at intermediate radii, where the surface density plateau or the maximum value of Σ_{HI} are reached, but close to the centre, the GK11 method generally results in more depressed profiles (but see Au 11, Au 13, Au 26 for the opposite trend). In Section 4.5, we discuss in more detail what these differ-

ences imply for the global properties (such as the total HI mass) and scaling relations of the simulated gas discs.

In Fig. 7 we show the median HI radial profiles for the 30 Auriga haloes computed with the L08 (blue symbols with error bars) and the GK11 (red symbols with error bars) prescriptions for estimating the molecular hydrogen fraction. The median values have been obtained by interpolating the profiles presented in Figs. 5 and 6 as a function of the galactocentric distance (normalized to R_{HI}) on to a uniformly spaced radial grid of width $0.1 \times R/R_{\mathrm{HI}}$. Error bars indicate the region between the 16-th and 84-th percentiles of each radial bin of the simulated HI profiles. The simulation results are compared with the median profile (obtained with the same procedure) of the Bluedisk sample (Wang et al. 2014, grey solid line). The shaded grey area indicates again the region between the 16-th and 84-th percentiles in each radial bin of the observed Bluedisk radial profiles.

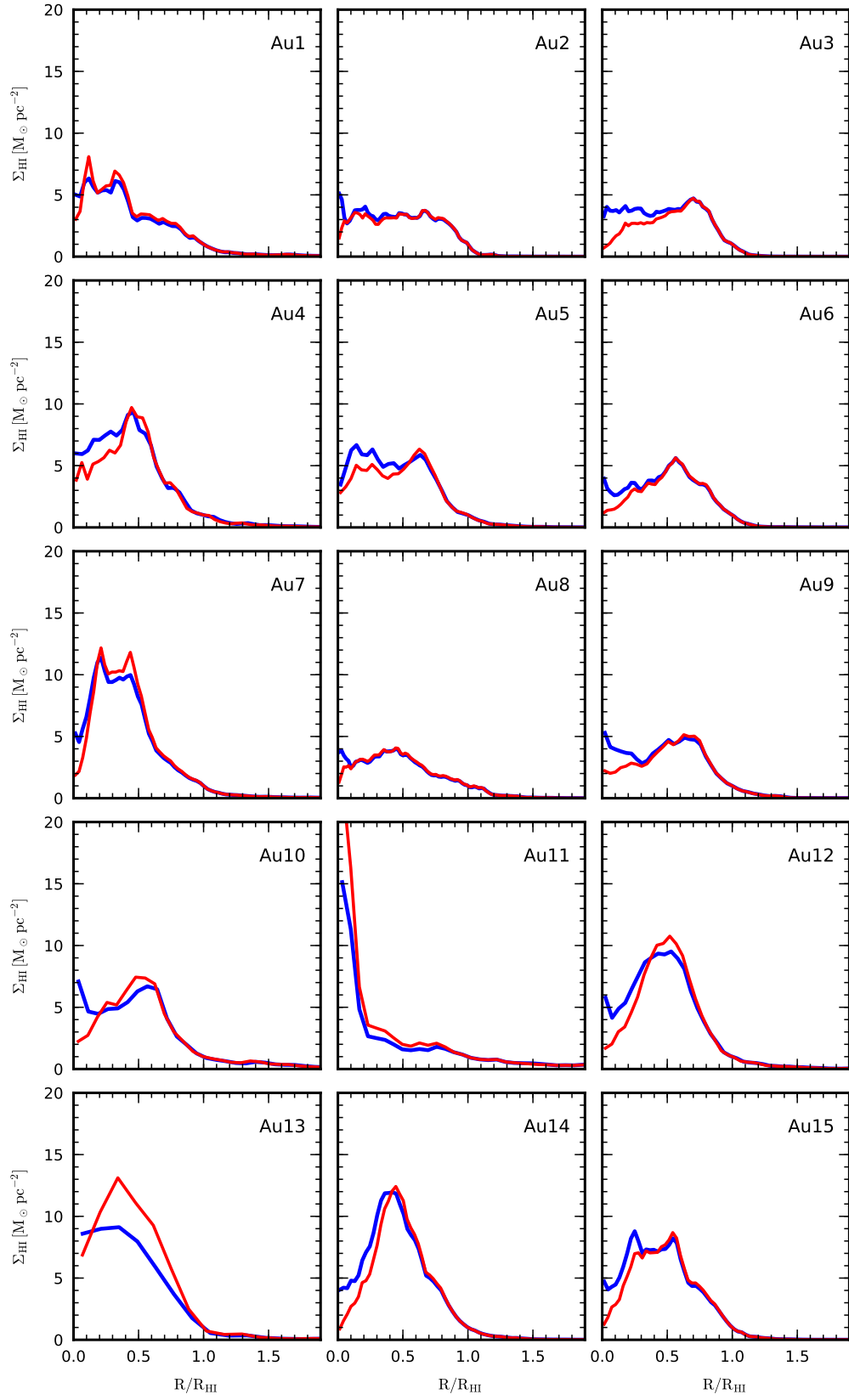A comparison between the median simulated profiles reveals

Figure 5. HI surface density profiles as a function of the galactocentric radius (in units of the HI radius of each galaxy, see Table 1) for haloes Au 1 to Au 15. The blue and red lines indicate the profiles obtained using the prescription from L08 or GK11 for removing molecular gas, respectively.
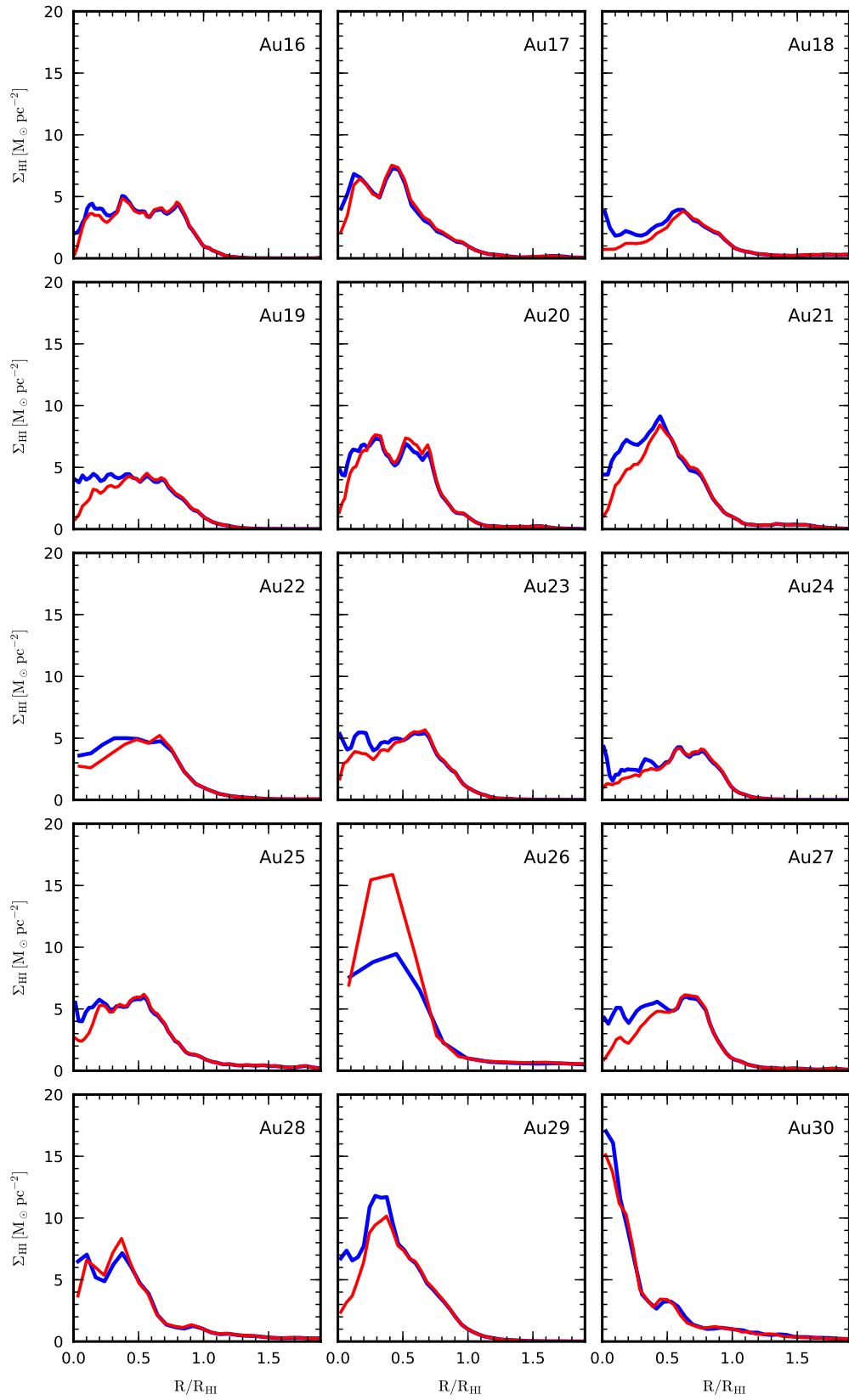
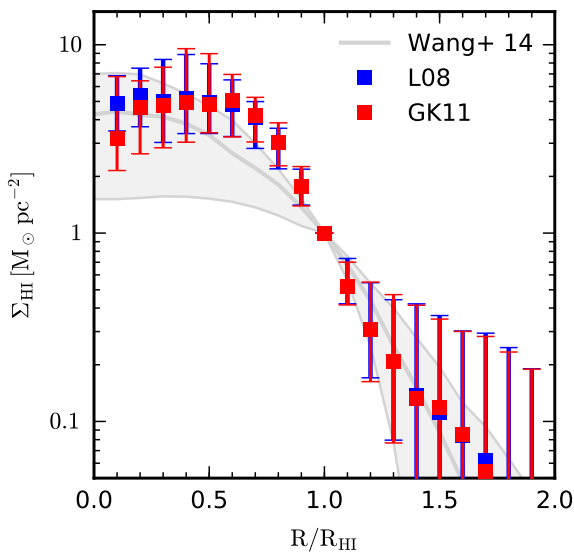**Figure 6.** As in Fig. 5, but for haloes Au 16 to Au 30.

Figure 7. Median H I profiles for the 30 Auriga haloes derived with the L08 (blue symbols) and GK11 (red symbols) prescriptions for the treatment of molecular hydrogen. For comparison, the median H I profile for the Bluedisk sample (Wang et al. 2014, grey lines) is shown. Error bars and the shaded grey region indicate the area between the 16-th and 84-th percentiles of each radial bin (of size $0.1\,R_{\rm HI}$) of the three distributions.

Figure 8. H I vertical thickness (defined as the height containing 75% of the H I mass) as a function of the SFR within the galaxy B-band optical radii for the 30 Auriga haloes derived with the L08 (blue symbols) and GK11 (red symbols) prescriptions for the treatment of molecular hydrogen. Dashed lines represent the best-fitting relations in the two cases, with parameters indicated in the legend.

that they are very similar at all radii, and that they start to differ only in the innermost regions where the GK11 profile starts to show a decrease in the H I surface density, which is however less marked than the one observed in the individual profiles. Compared to the Bluedisk sample, both the L08 and the GK11 median profiles are largely consistent with observations although some discrepancies are present. In particular, the simulated profiles overpredict the values of the H I surface density in the radial range $0.4 \lesssim R/R_{\rm HI} \lesssim 0.8$.

It is also instructive to compare our results with those found in the EAGLE simulations (B16), in which the more local and violent nature of the stellar feedback results in $\sim$ 10 kpc-scale holes in the (neutral) gas distribution. We note that H I holes have been observed in nearby disc galaxies, although they have more moderate sizes ($\sim$ 1 kpc), and are indeed interpreted as an effect of stellar feedback (Boomsma et al. 2008, and references therein). The presence of these large holes impacts the H I radial profiles of the EAGLE galaxies, with the result that in the central parts the median H I profile is underestimated with respect to the observations. The Auriga galaxies, thanks to a more distributed stellar feedback, do not suffer from this problem. In fact, they tend to overpredict the H I content at intermediate radii. Moreover, the discrepancies in the radial profiles (but also other H I related quantities; see the following sections) due to a different choice of the prescription used to model the contribution of molecular hydrogen are negligible in the Auriga case (except for a depletion of H I in the innermost regions), while in EAGLE they are significantly larger. Indeed, even considering a simulated galaxy sample in which big H I holes are not present, the GK11 method systematically underpredicts the H I surface density in the central region of the EAGLE galaxies, while equation (3) – with a slightly different choice of parameters than in the present work (see Blitz & Rosolowsky 2006) – reproduces the observations fairly well.
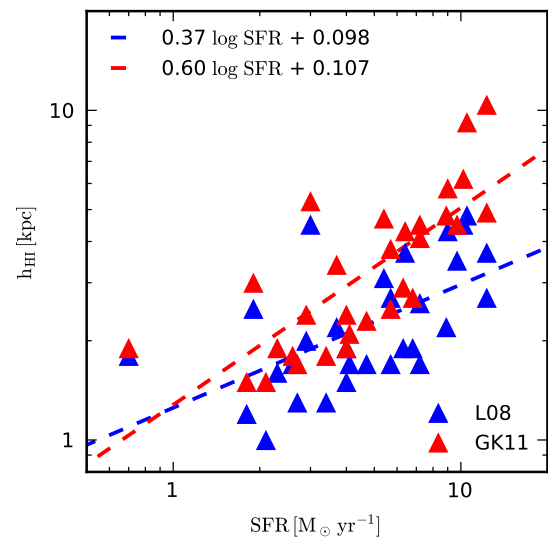
4.3 H I vertical distribution

We now focus on the vertical structure of our simulated H I discs. As it is apparent from the edge-on column density maps presented in Section 4.1, the vertical extent of the H I layer varies for each object. Here we want to analyse this variation in a more quantitative way and relate it to the internal properties of the central galaxy, in particular to its SFR. There are, of course, processes external to the galaxy that will also affect the vertical H I distribution, such as mergers (see e.g. the cases of Au 11 and Au 30) or close interactions with satellites (e.g. Au 18), which however we do not discuss in the present work (but see Gómez et al. 2016a,b, for an analysis of the impact of these effects on the vertical motion of gas and stars within galactic discs).

It is worth recalling that in our galaxy formation physics model, galactic outflows are powered by supernova explosions. The energy of these outflows is related to the global SFR of the galaxy. It is thus natural to expect a relation between this property and the structural properties of the H I disc, such as for instance the vertical thickness of the H I layer. Fig. 8 presents the corresponding correlation obtained with the two different methods we used to compute the molecular hydrogen mass fraction (blue symbols for the L08 and red symbols for the GK11 prescription, respectively) together with their best-fitting relations (dashed lines of the same colours). The best-fitting parameters are given in the legend. To select the actively star forming region of the galaxy, we consider only the region of the disc within the optical radius of the galaxy $R_{\rm opt}$, computed as the galactocentric radius at which the B-band surface brightness profile reaches $25\,{\rm mag\,arcsec}^{-2}$. We then estimate the total SFR of the galaxy and the H I mass in a cylinder of radius $R_{\rm opt}$, extending $\pm 30\,{\rm kpc}$ outside the disc plane. Finally, we define the H I vertical thickness $h_{\rm HI}$ as the height containing 75% of the H I mass determined in the step above. The inferred values of $h_{\rm HI}$ for both the L08 and GK11 methods are presented in Table 1.

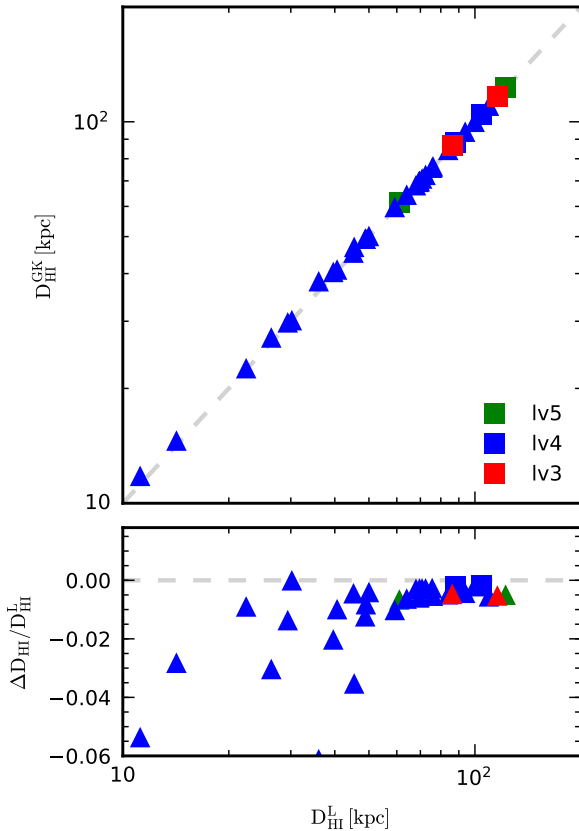Fig. 8 shows a correlation between the H I vertical thickness

Figure 9. H I diameter mass obtained by using the L08 and the GK11 prescription to account for the molecular gas for the 30 Auriga haloes. Top panel: comparison of the H I diameters obtained in the two cases. Bottom panel: fractional variation with respect to the L08 H I diameter as a function of the L08 H I diameter. Dashed lines in both panels show the 1:1 correspondence.

and the SFR of the central galaxy, with more actively star forming galaxies having larger values of h_{HI}. Overall, this relationship between the star forming properties of the galaxy and the thickness of its H I layer is consistent with the theoretical picture that galactic fountain flows generated by stellar feedback can push a significant fraction of the H I mass outside the galaxy mid-plane (see e.g. Fraternali & Binney 2006, 2008; Marasco & Fraternali 2011). This is also in agreement with the so-called upside-down disc formation scenario in which a declining SFR leads to a gas disc getting thinner with time (see Grand et al. 2016b, for a detailed analysis of this in a subsample of the Auriga haloes). The degree of scatter around the best-fitting relation is significant, supporting the idea that also external processes contribute to building of the H I layers. The correlation is present regardless of the technique used to estimate the molecular gas fractions in the simulations, but it is actually steeper – and the associated H I vertical thickness is larger – for the GK11 method. This can be explained the fact the GK11 model predicts in the central regions of the majority of the simulated galaxies a deficiency in the H I content with respect to the L08 model. However, the total H I masses are rather similar between the two methods (see Fig. 10), which implies that in the GK11 case more H I mass is found at larger vertical distances from the galaxy mid-plane.

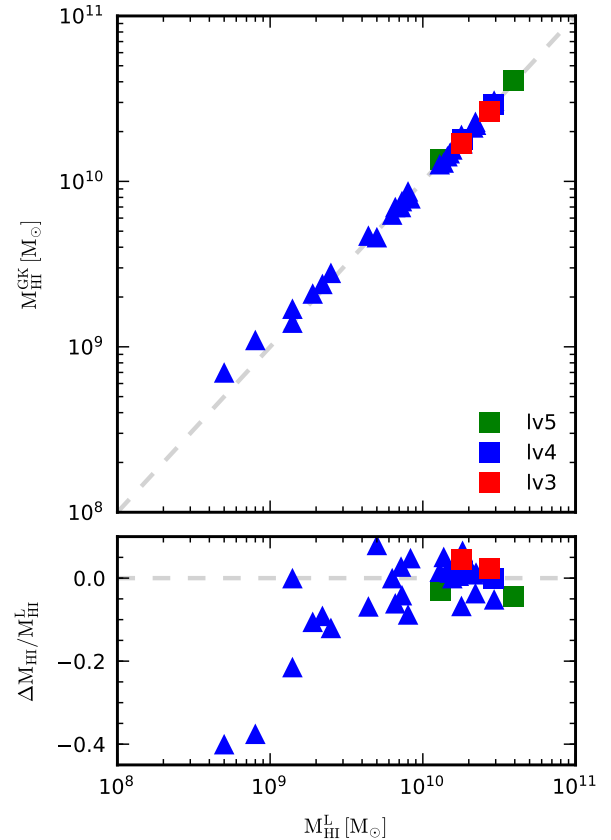Unfortunately, from the observational point of view there are

Figure 10. As in Fig. 9, but for the inferred H I mass of the Auriga sample.

not many examples for which there exists a robust estimate of the vertical scale-height of the extended H I layers. A list of edge-on galaxies for which this measure is available can be found in Zschaechner et al. (2015, and references therein). For this set of objects, scale-heights are typically in the range $\sim 0.2 - 2.5$ kpc. Before comparing these values with the Auriga findings, we caution the reader that there are different conventions for the H I scale-height used in observations, which depend on the functional form fitted to the vertical H I distribution and the use of one or multiple components in the fit, and those differ from the definition of vertical thickness that we have adopted in our work.

Keeping in mind these caveats, we can examine how the trends inferred from Auriga compare to two prototypical examples of galaxies in which a HI halo has been detected: the Milky Way and NGC 891. In the Milky Way, Marasco & Fraternali (2011) estimated a scale height of 1.6 kpc for a SFR of $\sim 3\,M_{\odot}\,yr^{-1}$ (Diehl et al. 2006), which is compatible with what we find in our analysis. The same applies to NGC 891, which has a scale height of about 2 kpc (Oosterloo et al. 2007) for a total SFR of $3.8\,M_{\odot}\,yr^{-1}$ (Popescu et al. 2004).

4.4 Differences in the global H I properties

From the profiles computed in Section 4.2 it is possible to derive the total H I mass of the galaxy as the mass of all the gas cells within R_{HI}. We report these values in Table 1 for all the 30 objects we

have simulated [3], together with their HI radii and the average HI surface density within R_{HI}, for the two different methods we have used to remove the contribution of molecular hydrogen.

Figs 9 and 10 illustrate the differences between the recovered HI diameters and HI masses, respectively, for both the L08 and GK11 methods to account for molecular hydrogen. The top panels of both figures present a direct comparison between the two methods, while the bottom panels show their fractional variation with respect to the L08 value. Different colours show simulations at different resolution levels (see Section 4.7 for more details), while the dashed lines indicate the 1:1 correspondence.

Let us first focus on $D_{HI} \equiv 2R_{HI}$. We have already mentioned in Section 4.2 that at large radii ($R \sim R_{HI}$) the method used to compute the molecular fraction has a negligible impact on the results. Therefore, it is not surprising that the HI diameters estimated with the two methods agree so well. Basically, all the simulated points lie very close to the 1:1 expectation. The fractional difference between the two D_{HI} values is of the order of a few per cent. The general outcome is that the GK11 method tends to recover slightly larger values for the HI diameter. There is no obvious trend of the fractional differences as a function of the HI size of the simulated objects, although it seems that they are more pronounced at smaller D_{HI}.

The same conclusions can be reached for the HI masses, although here the differences are larger (of the order of 10% and reaching up to 40% for small masses). However, in this case the fractional differences between the two masses are spread approximately evenly around the 1:1 value. This can be explained by the fact that the HI diameters recovered by the GK11 method are consistently larger than their L08 counterparts, which compensates for the smaller HI column densities found in the inner regions of the disc for the GK11 method. Again, there is no obvious trend in the fractional differences as a function of the HI mass, although the differences become more distinct at low M_{HI}.

4.5 The mass–diameter relation

An important scaling relation in HI observations of nearby disc galaxies is the one linking the total HI mass of the galaxy to the size of the HI disc, the so-called mass diameter relation (Broeils & Rhee 1997; Verheijen & Sancisi 2001; Swaters et al. 2002; Noordermeer et al. 2005; Martinsson et al. 2016). Fig. 11 shows this relation for our simulated sample of galaxies for the L08 (blue symbols) and the GK11 (red symbols) methods to account for the molecular hydrogen. Lines of the same colour show the best fit to this relation of the form

$$\log\left(\frac{M_{HI}}{M_\odot}\right) = \alpha \log\left(\frac{D_{HI}}{kpc}\right) + \beta, \qquad (8)$$

with the best-fitting parameters given in the legend. Grey lines indicate the best-fitting relations derived from observations of nearby galaxies (Verheijen & Sancisi 2001; Martinsson et al. 2016; Ponomareva et al. 2016). We also show, as empty symbols, observational results taken from the SPARC galaxy sample (Lelli et al. 2016) to give an indication of the observed scatter in the relation. Our simulated galaxies reproduce the same general trend seen in observations, in which a larger HI size corresponds to a higher HI mass, and they agree with the observed scaling relation(s) (right panel)
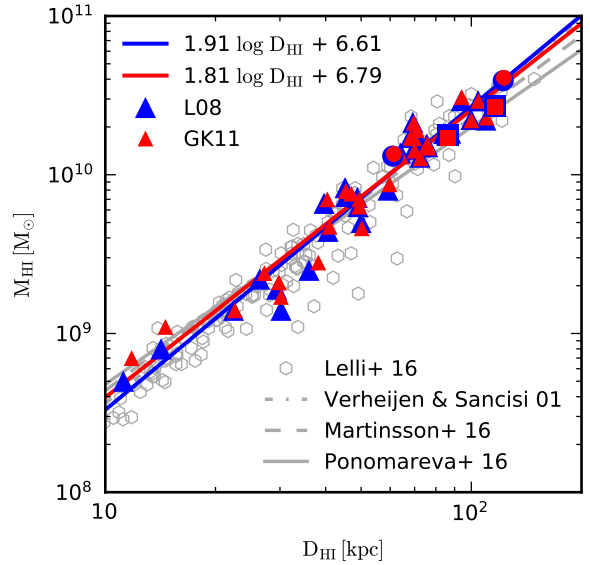

Figure 11. The HI mass diameter relation for the Auriga galaxies. Blue symbols show the results obtained with the empirical relation from L08 to account for molecular gas, while red symbols show the outcome of the prescription described in GK11 with lines of the same colours indicating the best-fitting relation inferred from the two samples. Gray lines and empty symbols, instead, compare the Auriga findings to observations of nearby galaxy as shown in the legend. Triangles present the results obtained at the standard (level 4) resolution, while circles and squares show haloes Au 16 and Au 24 at resolution levels 5 and 3, respectively a factor of 8 coarser or finer in mass resolution (see also Section 4.7).

very well. The agreement is good even in terms of the rms scatter in the relation ($\simeq 0.06$ dex in the residuals of the diameter distribution, see also Wang et al. 2016). Reassuringly, the variations in the best-fitting relations inferred from the simulated L08 and GK11 samples are small, the L08 relation being slightly steeper. They are consistent with the observational uncertainties affecting the determination of the best-fitting parameters from real data.

Our results on the mass-diameter relation are in agreement with the findings by B16, who report that EAGLE galaxies are consistent with the observational constraints. More precisely, B16 compare their simulated HI discs to the Broeils & Rhee (1997) best-fitting relation which is not shown in Fig. 11 but is equivalent (its slightly higher slope is compensated by a lower zero-point) to the ones considered in our analysis. Therefore, we conclude that, unlike the HI surface density radial profiles, the mass-diameter scaling relation is a very robust outcome of simulations, even for very different treatments of the star-forming gas and stellar feedback. However, contrary to the B16 analysis, we do not observe a dramatic change in slope of the mass-diameter relation in the GK11 case.

The above also implies that the average HI surface density within R_{HI} is an approximately constant or slowly declining function of the HI diameter in the Auriga galaxies in agreement with observations. Although there is considerably more scatter in this relation, its amplitude and the variability of the best fitting parameters are consistent with the observational findings.

---

[3] Data are also available in electronic format at http://auriga.h-its.org/data.html
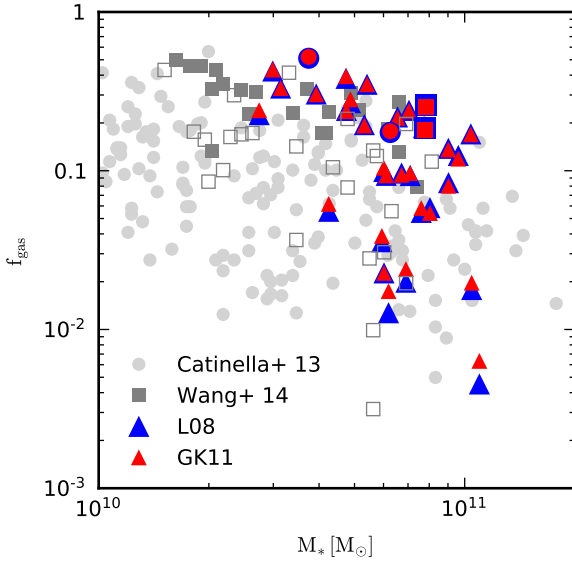
Figure 12. H I gas fraction as a function of the stellar mass for the Auriga sample. Stellar masses are computed within 10% of the virial radius of each object, while H I masses are those listed in Table 1. Results obtained through the empirical relation in L08 to account for molecular gas are shown with red symbols, while those obtained by applying the GK11 prescription are represented by blue symbols. Triangles give the results obtained at the standard (level 4) resolution, while circles and squares show haloes Au 16 and Au 24 at resolution levels 5 and 3, respectively a factor of 8 coarser or finer in mass resolution (see also Section 4.7). Grey symbols indicate observational findings from the GASS (Catinella et al. 2013) and the Bluedisk (Wang et al. 2014) surveys, as indicated in the legend. For the combined data sets, only 195 out of 300 galaxies which were significantly detected in H I are shown.

4.6   Gas fractions

In Fig. 12 we present the H I gas fractions [$f_{\mathrm{gas}} \equiv M_{\mathrm{HI}}/(M_\star + M_{\mathrm{HI}})$] as a function of the stellar mass for the Auriga sample. Stellar masses are computed within 10% of the virial radius of each object (see also Marinacci et al. 2014a; Grand et al. 2016a), and the H I gas masses are those reported in Table 1. Different colours indicate the two different methods to compute the contribution of molecular hydrogen, as indicated in the legend. The simulation results are compared to galaxies significantly detected in H I in both the GALEX Arecibo SDSS Survey (GASS, Catinella et al. 2013) and Bluedisk (Wang et al. 2013) samples. The Bluedisk sample is further split between gas-rich galaxies (full symbols) and a control sample (empty symbols), as in Wang et al. (2013).

Although the simulated range in stellar masses is somewhat reduced compared to observations – remember that the Auriga haloes were selected to be a match for the Milky Way – the Auriga set shows a declining H I gas fraction for increasing stellar mass as in the observations. The decline in the gas fraction is comparable to the observations, with an abrupt decrease at $M_\star \sim 6 \times 10^{10} \mathrm{M}_\odot$ where f_{gas} drops from 10% to about 1%. These trends are robust with respect to the model used to compute the molecular hydrogen fraction with almost no difference in the recovered gas fractions, except at the very high end of the stellar mass spectrum where, however, the difference is within a factor of 2.

A comparison to the observations indicates that the Auriga galaxies are systematically more gas-rich than the average for their stellar mass. If one considers the GASS sample, it can be readily seen that the Auriga set is at the upper envelope of the observed galaxies. If, instead, the Bluedisk sample is considered, the simulated galaxies follow more closely the trend of the gas-rich sample (which notably is composed of galaxies with H I mass fractions 0.6 dex higher than the median relation found in Catinella et al. 2010) than the one of the control sample comprising more 'average' galaxies. This occurs for stellar masses below the value $M_\star \sim 6 \times 10^{10} \mathrm{M}_\odot$. As already discussed above, for stellar masses larger than this value, f_{gas} drops quite abruptly to the 1% level. While being consistent with the gas fractions observed in galaxies detected in H I, this value is not representative of the global galaxy population given the numerous non-detections present in the two samples that are not shown in the figure (about one third of the total targeted galaxies).

The fact that the Auriga galaxies are generally more gas-rich than the observations should not be surprising given the results already discussed in Sections 4.2 and 4.5, in which we showed that our simulations overpredict the average surface density of the H I discs and preferentially populate the high-mass, large-size part of the mass-diameter relation. Given that the stellar masses recovered by the Auriga project are consistent with abundance matching predictions (Grand et al. 2016a), we have investigated whether this higher H I content might be due to the fact that the method presented in Section 3.1 does not apply any correction for photoionization (originating from the cosmic UV background and the local stellar radiation field) to the star-forming gas, thus overestimating its neutral gas fraction. The contribution of this gas phase to the total H I content of the Auriga galaxies is highly variable, ranging from $\sim 10\%$ to being the predominant contribution to the HI mass ($\gtrsim 95\%$) in the most compact galaxies such as Au 26 and Au 13. On average the contribution of star-forming gas to the total H I mass is about 45%. Therefore, applying a correction for photoionisation to the star-forming gas might alleviate the tension with the observations on the gas content of the Auriga galaxies, especially in the case of less extended H I discs. To further study this issue, it would also be informative to check whether the observational trends, including H I non-detections, could be better reproduced by a more general population of simulated haloes not chosen to be a match for the Milky Way, in line with what has been achieved in uniformly-sampled cosmological boxes such as EAGLE (B16; Crain et al. 2016).

4.7   Resolution dependence

Up to now we have used our fiducial resolution level to analyse the H I properties of the Auriga galaxies. A few selected galaxies in the Auriga set have been re-simulated also at different mass and spatial resolution levels. These additional simulations have been performed with the same galaxy formation physics model as the fiducial runs; only the number of resolution elements in the high-resolution region (and consequently the force resolution of the simulations) has been modified. In this section, we are interested in checking how robust the results of our H I analysis are with respect to a change in the resolution of the runs.

We first introduce a naming convention for easy reference to runs differing only in numerical resolution. Following the nomenclature adopted in the Aquarius project (Springel et al. 2008), we identify each resolution level with a numeral. A difference of one resolution level means a finer (or coarser) mass resolution by a factor of 8, thus implying a spatial resolution (i.e. a softening length) which can be finer (or coarser) by a factor of 2. The lower the numeral identifying the resolution level, the finer the effective (mass
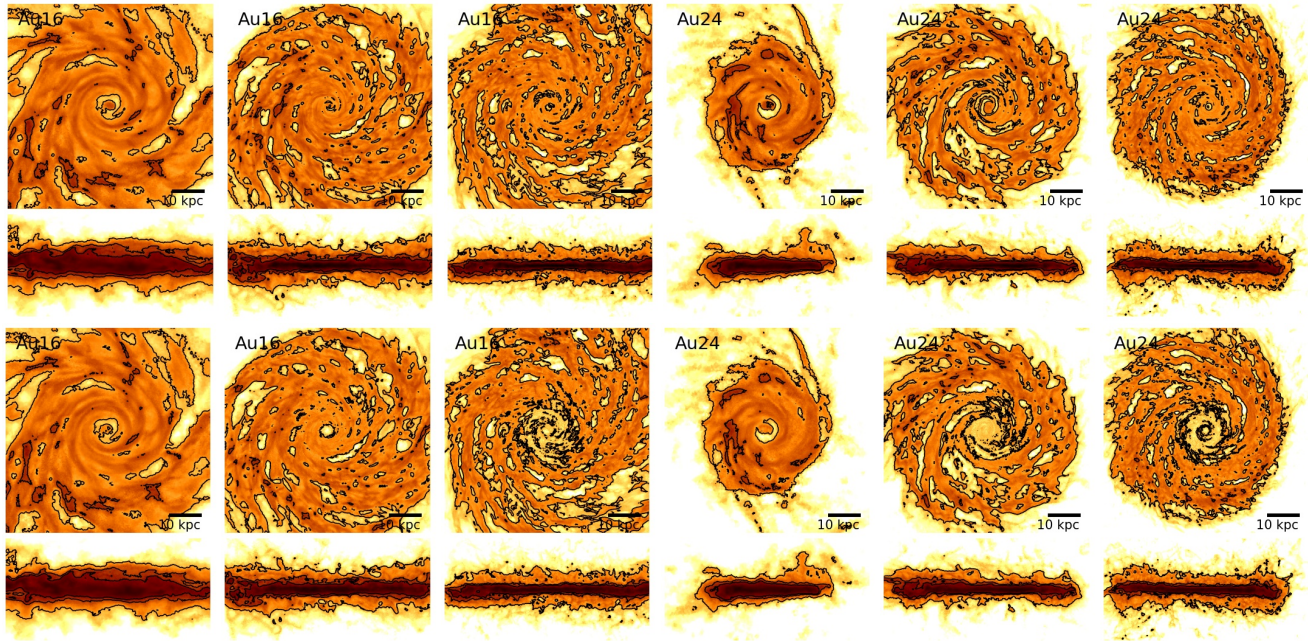
Figure 13. Resolution study for the H I column density maps of haloes Au 16 and Aq 24. From left to right and for each halo, the resolution level varies from the least resolved to the most resolved. The top row shows the maps obtained using the prescription from L08 for removing molecular gas, while the H I maps in the bottom row adopt the GK11 approach. The size of the projected region is 90 kpc on a side for face-on projections and 90×45 kpc for the edge-on ones.

and spatial) resolution. In what follows, we are going to analyse three different resolution levels for the haloes Au 16 and Au 24: our fiducial runs at resolution level 4, and finer (level 3) and coarser (level 5) realizations.

Fig. 13 presents H I face-on and edge-on density projections (in a way akin to Figs 2–4) for the haloes Au 16 and Au 24. The top row in each figure shows the H I surface density obtained with the L08 prescription to compute the contribution of molecular hydrogen, while in the bottom row the GK11 model has been used. The resolution increases for each halo from left to right such that each column in the figure represents H I density projections of either halo Au 16 or Au 24 at the same resolution level but obtained with different treatments for molecular hydrogen.

From the figure, it can be seen that the main morphological traits of the H I discs are present for both haloes at all three different resolution levels. Not surprisingly, higher resolution brings out finer details in the gas distribution. In particular, in the edge-on projections it is apparent that the thin component of the H I disc is better defined at the highest resolution level, while the vertical gas distribution puffs up considerably at the lowest resolution. The central depletion in the H I content for the GK11 method is barely noticeable at the lowest resolution level for both haloes, but it is increasingly more visible at higher resolution – note how the size of the central H I 'hole' increases in size for the Au 16 halo. The most striking difference, however, concerns the radial extent of the H I disc in the halo Au 24. Indeed, at resolution level 5 the H I disc is significantly less extended than in the two higher resolution levels, where the size of the H I disc appears similar. Halo Au 16 is not affected by this discrepancy, and the variation of the disc size across the different resolution levels is smaller.

Fig. 14 presents H I surface density profiles as a function of the galactocentric radius (normalized to $R_{\rm HI}$) for haloes Au 16 (top) and Au 24 (bottom). Line colours show the results obtained with the L08 (blue) and GK11 (red) prescriptions to compute the molec-

ular hydrogen mass fraction, while their line-style identifies the resolution level as indicated in the legend. Light grey lines are the H I surface density profiles of the Bluedisk survey and are shown for comparison.

The H I radial profiles show the general trends already discussed in Section 4.2, that is an increasing H I surface density profile in the innermost regions which reaches a maximum value or a plateau and then quickly drops at $R \simeq 0.85 \times R_{\rm HI}$, leaving little gas past the H I radius of the galaxy. The H I surface density profiles are overall very similar across the resolution levels. Only level 5 presents marked differences with respect the two finer resolution levels, in particular for halo Au 24. In general, the profiles for level 4 and level 3 track one another closely, regardless of the prescription adopted to estimate the molecular gas fraction, although for halo Au 16 the level 4 profile predicts an H I column density about a factor of 2 larger than the corresponding level 3 profile at $R \sim 0.8 \times R_{\rm HI}$. A comparison of the simulated profiles with those obtained in the Bluedisk survey shows that the profiles of the Auriga galaxies are consistent with the observed ones, although occasionally (e.g. for halo Au 16 at level 4 and halo Au 24 at level 5) there is an excess of H I at $R \simeq 0.8 \times R_{\rm HI}$.

Starting from the radial H I density profiles it is possible to derive the structural properties of the H I discs (sizes, total masses and average densities) at the additional resolution levels in the same way as done for the fiducial resolution. We report these values in Table 1 under separate headings for the different resolution levels. Clearly, it is possible to investigate several scaling relation between these quantities, as already done in Sections 4.4 to 4.6, allowing us to check the robustness of our findings with respect to resolution changes. To this end, we added the relevant data points for haloes Au 16 and Au 24 at resolution levels 5 and 3 to the plots presented above, either in different colours (Figs. 9 and 10) or with different symbols (circles for level 5 and squares for level 3; see Figs 11 and 12). Although differences between the sizes, masses and aver-
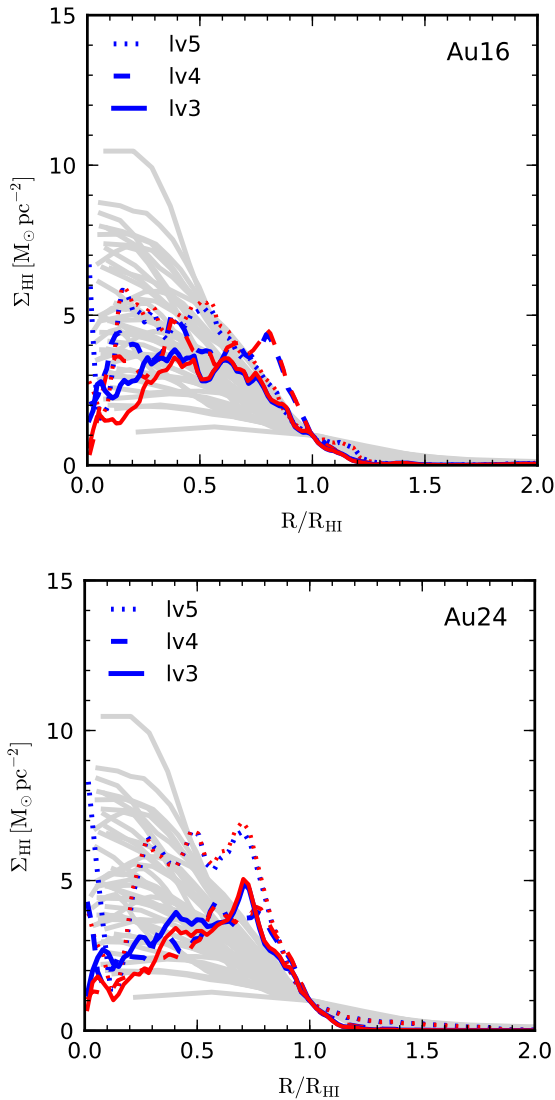
Figure 14. Resolution study for the H I surface density profiles for haloes Au 16 and Au 24. The blue and red lines indicate the profiles obtained using the prescription from L08 or GK11 for removing molecular gas, respectively. The line style indicates the resolution level, as given in the legend. Light grey lines display the H I radial profiles of the Bluedisk survey (Wang et al. 2014).

age densities exist across the three resolution levels, the individual data points follow the general pattern determined by the full set of 30 simulations at resolution level 4, meaning that each individual galaxy follows the general scaling relations derived for the full sample.

From these considerations we can conclude that our findings are robust with respect to changes in mass resolution (over a factor of 64) and this holds regardless of the prescription adopted to estimate the contribution of the molecular gas to the total neutral hydrogen density. While some discrepancies do exist between the different resolution levels, they tend to decrease with increasing resolution. In particular, our fiducial resolution level seems to be adequate to model the H I content of Milky Way-like systems with sufficient accuracy.

5   SUMMARY AND CONCLUSIONS

In this paper we have analysed the properties of the H I distribution in the Auriga simulations, a set of cosmological MHD simulations run with the moving-mesh code AREPO that investigate the formation and evolution of disc galaxies similar to our own Milky Way. We have modelled the H I gas by computing the neutral hydrogen fraction separately for low-density and star-forming gas, which, in the star formation module currently implemented in our simulations, is described by an effective equation of state and thus requires a special treatment to calculate its neutral fraction in a meaningful way. To estimate the contribution of molecular gas to the total neutral hydrogen mass we have used two different prescriptions – motivated by observational and theoretical studies – and compared their outcomes. Our main results can be summarized as follows.

(i) The vast majority of the simulated systems feature an extended (i.e. more extended than the associated stellar distribution) H I disc which in some cases may reach a radial extent of $\sim 60\,\mathrm{kpc}$. A few objects (i.e. Au 11 and Au 30) present disturbed morphologies as a consequence of late-time galaxy interactions.

(ii) The vertical extent of the H I distribution varies on a system by system basis. The amount of H I gas outside the disc plane correlates with the amount of star formation occurring in the (stellar) disc, in agreement with a scenario where most of the extra-planar H I gas results from a fountain-like gas flow (Fraternali & Binney 2006, 2008; Marasco & Fraternali 2011).

(iii) The (face-on) radial profiles of the H I surface density show a common pattern in which the H I surface density stays approximately constant and then exponentially drops at $\sim R_{\mathrm{HI}}$. Contrary to previous theoretical studies (B16), which however employed a substantially lower resolution than Auriga, our simulated galaxies do not show a deficiency of H I in the central region, but rather overpredict the H I contents at galactocentric radii $R \simeq 0.5\,R_{\mathrm{HI}}$.

(iv) Our simulated H I discs lie on the observed mass-diameter relation (e.g. Broeils & Rhee 1997). The scatter in the mass-diameter relation and the distribution of the average H I surface density within the H I radius are also consistent with those derived for a number of observational data sets (Verheijen & Sancisi 2001; Lelli et al. 2016; Martinsson et al. 2016; Ponomareva et al. 2016).

(v) The H I gas content in the Auriga galaxies, expressed in terms of gas fractions, is a declining function of the stellar mass present in the system, in agreement with observational findings. Compared to observations, our H I fractions are at the upper end of the allowed observational range, indicating that our simulated systems are systematically more gas-rich than typical nearby galaxies.

(vi) The main results of our analysis are robust with respect to changes in the prescription used to estimate the contribution of molecular hydrogen to the total neutral hydrogen mass, although the use of the GK11 model yields H I surface densities that are lower in the central regions than those estimated via the empirical H I/H_2 mass ratio relation of L08.

(vii) Our findings are slightly sensitive to variations in numerical resolution, but we note that the results for the two finer resolution levels are in good agreement with one another. Notwithstanding that, even the simulations run at the coarsest resolution level result in systems having H I distributions whose properties are consistent with the observational trends.

Our analysis exemplifies the significant progress achieved by cosmological simulations of galaxy formation – and especially with respect to the formation of galaxies similar to our own Milky Way – which can now not only reproduce important structural properties

(such as stellar masses, disc scale lengths and SFRs) and scaling relations associated with the stellar component of late type systems, but are also able to make meaningful predictions for the (neutral) gas component within the main galaxy. The predictions of these properties can be used, in conjunction with an accurate comparison to observations, to put new and more stringent constraints to the sub-grid physics used in these calculations, which is one of the major sources of uncertainties in current cosmological simulations.

In addition, having simulated gaseous discs whose properties are in broad agreement with the observed trends in nearby disc galaxies, one can now pursue interesting new lines of research. One promising direction in the context of the HI gas would be to carry out detailed studies of its dynamical state. This is an already well established observational field in radio astronomy for which many techniques have been developed and tested. The same techniques can now be systematically applied to simulation data, likely yielding informative comparisons between the simulated galaxies and the observations, an avenue that we intend to explore in future work.

REFERENCES

Aumer M., Binney J. J., 2009, MNRAS, 397, 1286
Aumer M., White S. D. M., Naab T., Scannapieco C., 2013, MNRAS, 434, 3142
Bahé Y. M., et al., 2016, MNRAS, 456, 1115
Barnes J., Hut P., 1986, Nature, 324, 446
Battaglia G., et al., 2005, MNRAS, 364, 433
Blitz L., Rosolowsky E., 2006, ApJ, 650, 933
Bonatto C., Bica E., 2011, MNRAS, 415, 2827
Boomsma R., Oosterloo T. A., Fraternali F., van der Hulst J. M., Sancisi R., 2008, A&A, 490, 555
Broeils A. H., Rhee M.-H., 1997, A&A, 324, 877
Catinella B., et al., 2010, MNRAS, 403, 683
Catinella B., et al., 2013, MNRAS, 436, 34
Chiappini C., Matteucci F., Gratton R., 1997, ApJ, 477, 765
Chiappini C., Matteucci F., Romano D., 2001, ApJ, 554, 1044
Colín P., Avila-Reese V., Roca-Fàbrega S., Valenzuela O., 2016, ApJ, 829, 98
Crain R. A., et al., 2016, preprint, (arXiv:1604.06803)
Dalla Vecchia C., Schaye J., 2012, MNRAS, 426, 140
Davé R., Katz N., Oppenheimer B. D., Kollmeier J. A., Weinberg D. H., 2013, MNRAS, 434, 2645
Dehnen W., McLaughlin D. E., Sachania J., 2006, MNRAS, 369, 1688
Diehl R., et al., 2006, Nature, 439, 45

Faucher-Giguère C.-A., Lidz A., Zaldarriaga M., Hernquist L., 2009, ApJ, 703, 1416
Fraternali F., 2009, in Andersen J., Nordströara m B., Bland-Hawthorn J., eds, IAU Symposium Vol. 254, The Galaxy Disk in Cosmological Context. pp 255–262 (arXiv:0807.3365), doi:10.1017/S1743921308027671
Fraternali F., 2014, in Feltzing S., Zhao G., Walton N. A., Whitelock P., eds, IAU Symposium Vol. 298, Setting the scene for Gaia and LAMOST. pp 228–239 (arXiv:1310.2956), doi:10.1017/S1743921313006418
Fraternali F., Binney J. J., 2006, MNRAS, 366, 449
Fraternali F., Binney J. J., 2008, MNRAS, 386, 935
Fraternali F., Marasco A., Armillotta L., Marinacci F., 2015, MNRAS, 447, L70
Giovanelli R., Haynes M. P., 2016, A&ARv, 24, 1
Gnedin N. Y., Kravtsov A. V., 2011, ApJ, 728, 88 (GK11)
Gómez F. A., White S. D. M., Grand R. J. J., Marinacci F., Springel V., Pakmor R., 2016a, preprint, (arXiv:1606.06295)
Gómez F. A., White S. D. M., Marinacci F., Slater C. T., Grand R. J. J., Springel V., Pakmor R., 2016b, MNRAS, 456, 2779
Grand R. J. J., et al., 2016a, preprint, (arXiv:1610.01159)
Grand R. J. J., Springel V., Gómez F. A., Marinacci F., Pakmor R., Campbell D. J. R., Jenkins A., 2016b, MNRAS, 459, 199
Guedes J., Callegari S., Madau P., Mayer L., 2011, ApJ, 742, 76
Habing H. J., 1968, Bull. Astron. Inst. Netherlands, 19, 421
Heald G., et al., 2011, A&A, 526, A118
Houck J. C., Bregman J. N., 1990, ApJ, 352, 506
Hunter J. D., 2007, Computing In Science & Engineering, 9, 90
Ikeuchi S., Ostriker J. P., 1986, ApJ, 301, 522
Kalberla P. M. W., Burton W. B., Hartmann D., Arnal E. M., Bajaja E., Morras R., Pöppel W. G. L., 2005, A&A, 440, 775
Katz N., Hernquist L., Weinberg D. H., 1992, ApJ, 399, L109
Katz N., Weinberg D. H., Hernquist L., 1996, ApJS, 105, 19
Lagos C. d. P., et al., 2015, MNRAS, 452, 3815
Lelli F., McGaugh S. S., Schombert J. M., 2016, AJ, 152, 157
Leroy A. K., Walter F., Brinks E., Bigiel F., de Blok W. J. G., Madore B., Thornley M. D., 2008, AJ, 136, 2782 (L08)
Li Y.-S., White S. D. M., 2008, MNRAS, 384, 1459
Macciò A. V., Udrescu S. M., Dutton A. A., Obreja A., Wang L., Stinson G. R., Kang X., 2016, MNRAS, 463, L69
Marasco A., Fraternali F., 2011, A&A, 525, A134
Marasco A., Debattista V. P., Fraternali F., van der Hulst T., Wadsley J., Quinn T., Roškar R., 2015, MNRAS, 451, 4223
Marasco A., Crain R. A., Schaye J., Bahé Y. M., van der Hulst T., Theuns T., Bower R. G., 2016, MNRAS, 461, 2630
Marinacci F., Binney J., Fraternali F., Nipoti C., Ciotti L., Londrillo P., 2010, MNRAS, 404, 1464
Marinacci F., Fraternali F., Nipoti C., Binney J., Ciotti L., Londrillo P., 2011, MNRAS, 415, 1534
Marinacci F., Pakmor R., Springel V., 2014a, MNRAS, 437, 1750
Marinacci F., Pakmor R., Springel V., Simpson C. M., 2014b, MNRAS, 442, 3745
Marinacci F., Vogelsberger M., Mocz P., Pakmor R., 2015, MNRAS, 453, 3999
Martinsson T. P. K., Verheijen M. A. W., Bershady M. A., Westfall K. B., Andersen D. R., Swaters R. A., 2016, A&A, 585, A99
McCarthy I. G., Schaye J., Font A. S., Theuns T., Frenk C. S., Crain R. A., Dalla Vecchia C., 2012, MNRAS, 427, 379
Navarro J. F., Steinmetz M., 1997, ApJ, 478, 13
Noordermeer E., van der Hulst J. M., Sancisi R., Swaters R. A., van Albada T. S., 2005, A&A, 442, 137
Oosterloo T., Fraternali F., Sancisi R., 2007, AJ, 134, 1019
Pakmor R., Marinacci F., Springel V., 2014, ApJ, 783, L20
Pakmor R., Springel V., Bauer A., Mocz P., Munoz D. J., Ohlmann S. T., Schaal K., Zhu C., 2016, MNRAS, 455, 1134
Peñarrubia J., Gómez F. A., Besla G., Erkal D., Ma Y.-Z., 2016, MNRAS, 456, L54
Planck Collaboration et al., 2014, A&A, 571, A16

Ponomareva A. A., Verheijen M. A. W., Bosma A., 2016, MNRAS, 463, 4052

Popescu C. C., Tuffs R. J., Kylafis N. D., Madore B. F., 2004, A&A, 414, 45

Popping A., Davé R., Braun R., Oppenheimer B. D., 2009, A&A, 504, 15

Powell K. G., Roe P. L., Linde T. J., Gombosi T. I., De Zeeuw D. L., 1999, Journal of Computational Physics, 154, 284

Rahmati A., Pawlik A. H., Raičevič M., Schaye J., 2013, MNRAS, 430, 2427

Roberts M. S., 1975, Radio Observations of Neutral Hydrogen in Galaxies. the University of Chicago Press, p. 309

Sakamoto T., Chiba M., Beers T. C., 2003, A&A, 397, 899

Sancisi R., Fraternali F., Oosterloo T., van der Hulst T., 2008, A&ARv, 15, 189

Schaye J., 2001, ApJ, 562, L95

Schaye J., et al., 2015, MNRAS, 446, 521

Shapiro P. R., Field G. B., 1976, ApJ, 205, 762

Springel V., 2005, MNRAS, 364, 1105

Springel V., 2010, MNRAS, 401, 791

Springel V., Hernquist L., 2003, MNRAS, 339, 289

Springel V., et al., 2008, MNRAS, 391, 1685

Stinson G. S., Brook C., Macciò A. V., Wadsley J., Quinn T. R., Couchman H. M. P., 2013, MNRAS, 428, 129

Swaters R. A., van Albada T. S., van der Hulst J. M., Sancisi R., 2002, A&A, 390, 829

Twarog B. A., 1980, ApJ, 242, 242

Verheijen M. A. W., Sancisi R., 2001, A&A, 370, 765

Vogelsberger M., Genel S., Sijacki D., Torrey P., Springel V., Hernquist L., 2013, MNRAS, 436, 3031

Vogelsberger M., et al., 2014a, MNRAS, 444, 1518

Vogelsberger M., et al., 2014b, Nature, 509, 177

Wakker B. P., 2004, in van Woerden H., Wakker B. P., Schwarz U. J., de Boer K. S., eds, Astrophysics and Space Science Library Vol. 312, High Velocity Clouds. p. 25, doi:10.1007/1-4020-2579-3˙2

Wakker B. P., van Woerden H., 1997, ARA&A, 35, 217

Walker A. P., Gibson B. K., Pilkington K., Brook C. B., Dutta P., Stanimirović S., Stinson G. S., Bailin J., 2014, MNRAS, 441, 525

Wang J., et al., 2013, MNRAS, 433, 270

Wang J., et al., 2014, MNRAS, 441, 2159

Wang L., Dutton A. A., Stinson G. S., Macciò A. V., Penzo C., Kang X., Keller B. W., Wadsley J., 2015, MNRAS, 454, 83

Wang J., Koribalski B. S., Serra P., van der Hulst T., Roychowdhury S., Kamphuis P., Chengalur J. N., 2016, MNRAS, 460, 2143

Wilkinson M. I., Evans N. W., 1999, MNRAS, 310, 645

Xue X. X., et al., 2008, ApJ, 684, 1143

Zschaechner L. K., Rand R. J., Walterbos R., 2015, ApJ, 799, 61